Accepted Manuscript

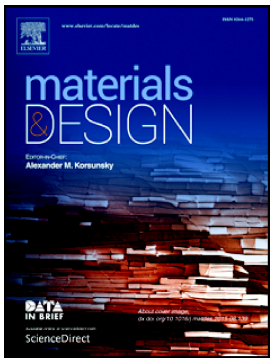

H13–partially stabilized zirconia nanocomposites fabricated by high-energy mechanical milling and selective laser melting

Faraz Deirmina, Bandar AlMangour, Dariusz Grzesiak, Massimo Pellizzari

PII:	S0264-1275(18)30189-8
DOI:	doi:10.1016/j.matdes.2018.03.017
Reference:	JMADE 3759
To appear in:	*Materials & Design*
Received date:	28 December 2017
Revised date:	26 February 2018
Accepted date:	7 March 2018

Please cite this article as: Faraz Deirmina, Bandar AlMangour, Dariusz Grzesiak, Massimo Pellizzari , H13–partially stabilized zirconia nanocomposites fabricated by high-energy mechanical milling and selective laser melting. The address for the corresponding author was captured as affiliation for all authors. Please check if appropriate. Jmade(2017), doi:10.1016/j.matdes.2018.03.017

H13–Partially Stabilized Zirconia Nanocomposites Fabricated by High-Energy Mechanical Milling and Selective Laser Melting

Faraz Deirmina [a], Bandar AlMangour [b*], Dariusz Grzesiak [c], Massimo Pellizzari [a]

[a] Department of Industrial Engineering, University of Trento, Trento, Italy

[b] School of Engineering and Applied Sciences, Harvard University, Cambridge, MA 02138, USA

[c] Department of Mechanical Engineering and Mechatronics, West Pomeranian University of Technology, Szczecin, Poland

[*]Corresponding author. Email: balmangour@seas.harvard.edu, balmangour@gmail.com

Abstract

This work demonstrated the feasibility of producing partially stabilized zirconia (PSZ)-reinforced AISI H13 steel composites through mechanical milling (MM) and selective laser melting (SLM). The effects of the energy of MM and SLM energy density on the density, microstructure, phases, and microhardness were investigated. Increasing the energy density (η) generally enhanced densification. However, high energy density and increased thermal stresses led to more spherical pores and thermal microcracks. All samples in the as-built condition showed a large amount of retained austenite (RA), which decreased with decreasing energy density. PSZ particles segregated under all processing conditions due to different densities and thermal conductivities of the matrix and reinforcements. Large, string-like areas of segregated PSZ exhibited cracks and debonding in SLM-processed low-energy MM composite powders, whereas SLM-processed high-energy MM powders exhibited smaller segregated PSZ agglomerates with different morphology; most of the PSZ areas were crack-free and well bonded to the matrix. A limited interfacial reaction layer formed in the H13–PSZ composites. High-energy MM composite powders formed parts with higher relative densities and microhardness than low-energy MM powders. Considerable metastable tetragonal ZrO_2 formed in all composites, suggesting the potential transformation toughening effect of PSZ to increase the composite's fracture toughness.

Keywords: Selective Laser Melting (SLM); Mechanical Milling; Tool Steel Matrix Composite; AISI H13; Partially Stabilized Zirconia; Retained austenite.

1. Introduction

AISI H13 is a chromium hot-work tool steel that is widely used for tools, as well as dies for material extrusion, die casting, and forging, thanks to its high wear resistance, hardness, and toughness. This steel is usually quenched and tempered, after which its microstructure consists of tempered martensite together with dispersed secondary carbides. These carbides retard softening at elevated temperatures and guarantee high hot hardness (strength at high temperature) [1]. There is increasing demand for dies with higher resistance to abrasive wear for extruding lightweight metal matrix composites (e.g., pure Al and Al alloys reinforced with SiC) because the interaction of hard ceramic particles (HPs) with the die can severely damage the die and decrease its lifetime [2]. This has encouraged the development of particle-reinforced tool steel matrix composites (i.e., metal-matrix composites, MMCs) strengthened by incorporating hard ceramic particles. The design of MMCs aims to exploit the high toughness of the metallic matrix and the superior hardness of the hard particles to fabricate dies with excellent wear resistance [3]. Pagounis et al.

[4] showed that the incorporation of 12 vol% reinforcing particles (i.e., VC or Cr_3C_2) in a powder metallurgical (PM) hot-work tool steel increased the three-body abrasive wear resistance of the tool up to seven times relative to the resistance of the unreinforced matrix material. However, the fracture toughness of tool steel matrix composites is dramatically lower than that of the matrix material. Previous studies suggested that when a high-strength matrix is subjected to strain, the stress at the poles of the HPs becomes sufficiently high for the HPs to fracture or for the matrix/reinforcement interface to fail [5]–[7]. Moreover, due to the difference between the coefficients of thermal expansion of the matrix and reinforcement, a hydrostatic tensile field of stress will develop in the matrix upon cooling from the processing temperature, which in turn deviates the crack towards the matrix/reinforcement interface, thus decreasing the fracture toughness [4].

One way to ameliorate the negative influence of the reinforcements on the overall toughness of the composite may be to select ceramic reinforcements that show high fracture stress and acceptable fracture toughness. Partially stabilized zirconia (PSZ), first introduced by Garvie et al. [8], showed promising properties. Below 1170°C, pure zirconia transforms into a monoclinic structure (m-ZrO_2) from the tetragonal phase (t-ZrO_2), accompanied by a 3% to 5% volume expansion. In PSZ, dopants (e.g., Y_2O_3 or MgO) partially stabilize t-ZrO_2 at room temperature, which can transform into the stable phase (m-ZrO_2) through stress-induced martensitic transformation. As a result of the phase transformation, PSZ shows higher fracture toughness (i.e., K_{IC} ~ 8 MPa/m^2) than other ceramics because as a crack propagates, the strain energy around the crack tip can be dissipated by the stress-induced transformation of the metastable tetragonal phase (t-ZrO_2) into the stable monoclinic one (m-ZrO_2). An additional toughening mechanism has been proposed in view of the compressive strain fields that form around the crack tip because of the volume expansion resulting from the t-to-m transformation, which opposes the crack propagation [9]. In a PSZ-reinforced composite, the effective volumetric transformation strain (θ_T) in the entire composite is defined by Eq. 1 [10]

$$\theta_T = C\theta_T^P \quad (1)$$

where C is the volume fraction of transforming particles, and θ_T^P is the volumetric transformation strain of the un-constrained particles (i.e., when the particles are not constrained by the matrix). If the composite contains a small volume percent of the transforming phase (i.e., PSZ) and the stiffness of the matrix material does not exceed that of PSZ (E_{PSZ} ~ 210 GPa, $\nu = 0.3$), the effective volumetric transformation strain of the PSZ will be increased [9], [10]. The transformation toughening effect of PSZ is thus expected to increase the toughness of the AISI H13 tool steel matrix composite (E_{matrix} ~ 208 GPa).

Selective laser melting (SLM) is a powder-bed fusion additive manufacturing process for the fabrication of multi-functional parts [11]. SLM completely melts the material, which then rapidly solidifies, giving rise to several microstructural features such as grain refinement (improved strength), extended solid solubility, and hindered formation of inter-particle porosity (i.e., decreased process-induced porosity) [12]. Thus, this fast solidification during SLM is expected to enhance the mechanical properties of hot-work tool steels such as hardness, yield strength, and fracture toughness [11], [13]. In general, tool steels with high strength and low fracture toughness are highly susceptible to cracking; thus, they are challenging to process. Among different types of tool steels, AISI H13 tool steel shows very good processability in terms of achieving crack-free parts with high relative densities due to its alloy composition (especially its medium C content) [14]. Therefore, providing nearly fully dense structures (rel. density ~ 99%) is feasible by optimizing process parameters such as the feedstock quality, scanning strategy, and scan speed–laser power relationship. [15] A previous study showed limited but promising results demonstrating the feasibility of fabricating tool steel composites reinforced with ceramic particles via low-energy mechanical milling (LMM) and SLM [16]. By choosing the proper SLM process parameters, rapid solidification should achieve a very fine microstructure with a uniform distribution of reinforcing particles inside the matrix, resulting in increased strength due to the synergetic effects of Hall–Petch strengthening and dispersion hardening. However, one of the main problems in processing such composites by SLM was reported to be the presence of high porosity and other laser-induced defects [16].

In order to design a material with a homogenous distribution of HPs in a ductile matrix, a geometrical model based on the HP size (d_p) and matrix powder particle size (d_m) was proposed by Tan and Zhang [17]. This model includes the HP volume fraction (f) and the strain induced in the samples by a secondary process (i.e., extrusion and/or rolling). The model was extended by Sabirov et al. [18] for severe plastic deformation (SPD) processes that induce a large amount of shear strain (γ) in the sample (e.g., equal channel angular pressing). Based on this model, the HP distribution is expected to be homogenous when the HPs are not smaller than a critical size:

$$d_p \geq \frac{d_m}{\left[\left(\frac{\pi}{6f}\right)^{\frac{1}{3}}-1\right]\frac{\sqrt{R}}{1-R'}\gamma} \quad (2)$$

where R is the extrusion ratio and R' the reduction ratio during rolling. According to this equation, a large shear strain can effectively lower the critical HP size needed to homogenously distribute the HPs in the matrix. As an SPD method, high-energy MM (HMM) introduces a large amount of shear strain into the powders and is considered an appropriate processing route for producing composite powders with a very

uniform and homogeneous dispersion of ultrafine HPs embedded in a severely deformed ultrafine grained (UFG) metallic matrix [19], [20].

Starting from this point and following the work of AlMangour et al. [16], this paper further investigates the feasibility of SLM for HMM AISI H13–PSZ composite powders containing 10 to 20 vol% PSZ and by varying the energy density (E) [21], which combines multiple interdependent process parameters in SLM into a single term,

$$E = \frac{p}{vst} \tag{3}$$

where p is the laser power, v is the scanning speed, s is the hatch spacing, and t is the layer thickness.

To compare composites processed by LMM with unreinforced AISI H13, samples were selective laser melted under the same processing conditions.

2. Materials and Methods

2.1. Mechanical Milling

AISI H13 gas-atomized (AT) powders (Sandvik Osprey, 0.45% C, 1.62% Mo, 5.36% Cr, 1.1% V, 0.43% Mn, 0.94% Si, Fe bal.) were used as the matrix material. The particle size distribution is given by d_{10} = 19 µm, d_{50} = 31 µm, and d_{90} = 51 µm. The mean particle size of the commercially available 3 mol% yttria-PSZ (3Y-PSZ) powder (hereafter denoted by PSZ for simplicity) was 0.5 µm. The as-received PSZ powders were 64 vol% t-ZrO_2, 8 vol% cubic ZrO_2 (c-ZrO_2), and 28 vol% m-ZrO_2.

The steel and PSZ powders were mixed together with 0.2 wt% Kenolube (Hoganas AB) as the process control agent (PCA) in a Turbula mixer for 60 min. The volume percent of PSZ was set to 10 or 20 vol%. The mixtures were then mechanically milled (MM) using a Fritsch Pulverisette 6 planetary ball mill using 100Cr6 steel (65HRC) balls with a diameter of 10 mm. Two different milling scenarios were considered (i.e., LMM [16] and HMM). In the case of LMM, the disk rotational speed was 200 rpm, and the ball-to-powder weight ratio (BPR) was set to 5:1 (g/g). The total milling time was set to 8 h, which was performed over 32 cycles consisting of 15 min of MM followed by a 9 min pause in order to avoid overheating during MM. For HMM, a rotational speed of 450 rpm and BPR of 6.67:1 (g/g) were used, while the overall milling time was 3 h and 20 min, with interrupted milling cycles of 2 min followed by a 9 min pause. These HMM conditions were previously shown to yield nanocrystalline H13–PSZ composite powders with a very uniform dispersion of PSZ particles trapped inside the lamellas of the severely plastically deformed matrix [22].

2.2. Selective Laser Melting

From the as-received AT steel powders and MM composite powders, cylinders (10 mm × 4 mm) were processed using the SLM machine (model: MCP HEK REALIZER II). The scanning was performed in an alternate-hatching pattern, which means that after scanning each layer, the scanning laser was rotated by 90° before scanning the subsequent layer. The layer thickness (d) was set to 50 μm, and a hatch distance (h) of 120 μm was applied. In order to avoid oxidation, the chamber was filled with high-purity argon. Two different scanning speeds were selected (i.e., 166.7 and 250 mm/s) using the control program of the SLM machine in order to obtain two different laser energy densities of 100 J/mm^3 and 67 J/mm^3, respectively. Table 1 summarizes the specifications of the powder batches subjected to SLM processing in this work and their corresponding sample labels.

Table 1. Sample labels and descriptions

Sample label	3Y-PSZ (vol %)	MM type	Laser energy density (J/mm^3)
HMM (10%)-67	**10**	**High energy**	**67**
LMM (10%)-67	**10**	**Low energy**	**67**
HMM (10%)-100	**10**	**High energy**	**100**
LMM (10%)-100	**10**	**Low energy**	**100**
LMM (20%)-67	**20**	**Low energy**	**67**
LMM (20%)-100	**20**	**Low energy**	**100**
AT-67	**0**	**-**	**67**
AT-100	**0**	**-**	**100**

2.3. X-ray Diffraction Analysis

The phase constitution of the starting and MM powders, as well as the SLM samples, was studied by X-ray diffraction (XRD) analysis using an Italstructures (IPD3000) instrument equipped with Co Kα source (λ = 0.1788965 nm), except for the LMM composite powders, which were analyzed using a Cu Kα source (λ = 0.15418 nm). Data were analyzed using the Rietveld method (i.e., considering the area under the peak in proportion to the volume percent of the corresponding phase) and elaborated by MAUD (Materials Analysis Using Diffraction) software [23]. The mean crystallite size and the average lattice microstrain were calculated by the default line broadening method in MAUD corresponding to the "Delft" model [23]. This simple model ascribes Lorentzian broadening to the finite crystallite size and Gaussian

broadening to the microstrain. The results were used to determine the effects of the severe plastic deformation induced by MM and energy density on structural refinement of the MM composite powders and SLM-processed bulk samples, respectively.

2.4. Density Measurements

The density of the samples was measured according to ASTM EB962. The density of the composites was assumed to conform to the linear "rule of mixtures."[24] .

$$\rho_{composite} = \rho_{H13} f_{H13} + \rho_{reinforcement} f_{Reinforcement} \quad (4)$$

where ρ and f are the absolute density and volume fraction of each constituent, respectively. The values in the literature for the absolute densities of AISI H13 (7.76 g/cm^3) and PSZ (6.05 g/cm^3) were used.

2.5. Microhardness Measurements

At least six microhardness measurements were performed on powders with an applied load of 0.05 N, whereas microhardness measurements were conducted on carefully polished "side view" and "top view" cross-sections of SLM samples using an applied load of 0.1 N.

2.6. Microstructural Characterization

Samples were cut by precision micro-cutting with a diamond blade. Metallographic sections (i.e., side and top views with respect to the SLM build direction) were prepared by grinding with SiC papers up to 1200 grit followed by polishing with 3 μm and 1 μm cloths and chemical etching with Nital (5% nitric acid in ethanol solution). The microstructure was analyzed using an optical microscope (OM) and a scanning electron microscope (SEM). Semi-quantitative energy-dispersive X-ray spectroscopy (EDS), including line scan analysis and elemental mapping, was performed on the SLM samples to investigate the formation of thermodynamically plausible reaction products that may be formed in steel–PSZ systems upon processing these composites at high temperatures [25], [26].

2.7. Thermal post processing

H13 is usually quenched and tempered before use. Therefore, quenching treatments were conducted using a dilatometer (Bahr DIL805) to investigate the effects of energy density and PSZ addition on the quenched microstructure and phase constitution of the samples. The samples were mounted between quartz pushrods connected to a linear variable differential transformer (LVDT). The temperature of the sample was measured with a spot-welded thermocouple. The samples were heated to 1020°C (15 min

holding time) under a dynamic vacuum of 5×10^{-4} mbar and then quenched to room temperature at a constant cooling rate of 50 K/min.

3. Results and discussion

3.1. Powder Characterization

3.1.1 As-received gas-atomized (AT) powder

The AT powders show a spherical morphology, which is characteristic of the gas atomization process (Fig. 1a). The cellular structure observed in the metallographic cross-section of the powders features the microsegregation of several alloying elements due to the fast solidification of powders during gas atomization (Fig. 1b). The EDS analysis (Table 2) confirms the higher concentration of alloying elements in microsegregated areas.

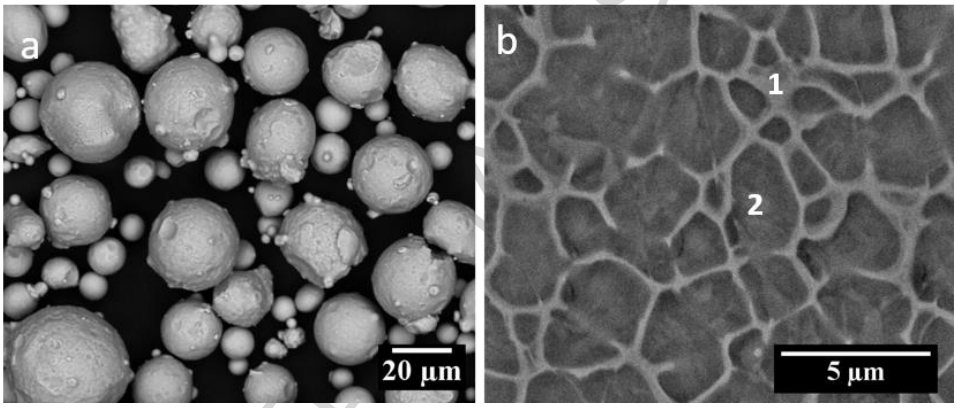

Figure 1. SEM micrographs of a) spherical gas-atomized H13 particles and b) back-scattered electrons (BSE) micrograph showing the cellular microstructure

Table 2. EDS elemental analysis results (in wt. %) on area (1) and spot (2) marked in Fig. (1b)

Elements/ Position	Fe	Cr	V	Mn	Mo	Si
Spot 1	**84.8**	**8.3**	**2.8**	**0.5**	**3.2**	**0.3**
Area 2	**91.8**	**5.3**	**1.2**	**0.4**	**0.9**	**0.3**

The average powder microhardness was around 690±10 HV0.05. The XRD results confirm the presence of 19 vol% retained austenite (RA) in AT powders (Fig. 2), which is softer than α-Fe. Moreover, the α-Fe mean crystallite size and microstrain were estimated to be 75±5 nm and 0.3%, respectively. The lattice parameter ratio (i.e., c/a) is slightly more than 1.000 (i.e., 0.2882/0.2879). In view of the very high

cooling rates of the gas atomization process (i.e., 10^4-10^6 K/s), which can be defined as intensive quenching, the melt is undercooled and the fast solidification starts under non-equilibrium conditions [27]. Therefore, the microhardness of the powders and the XRD results confirm the formation of the BCC martensite microstructure after the gas atomization process.

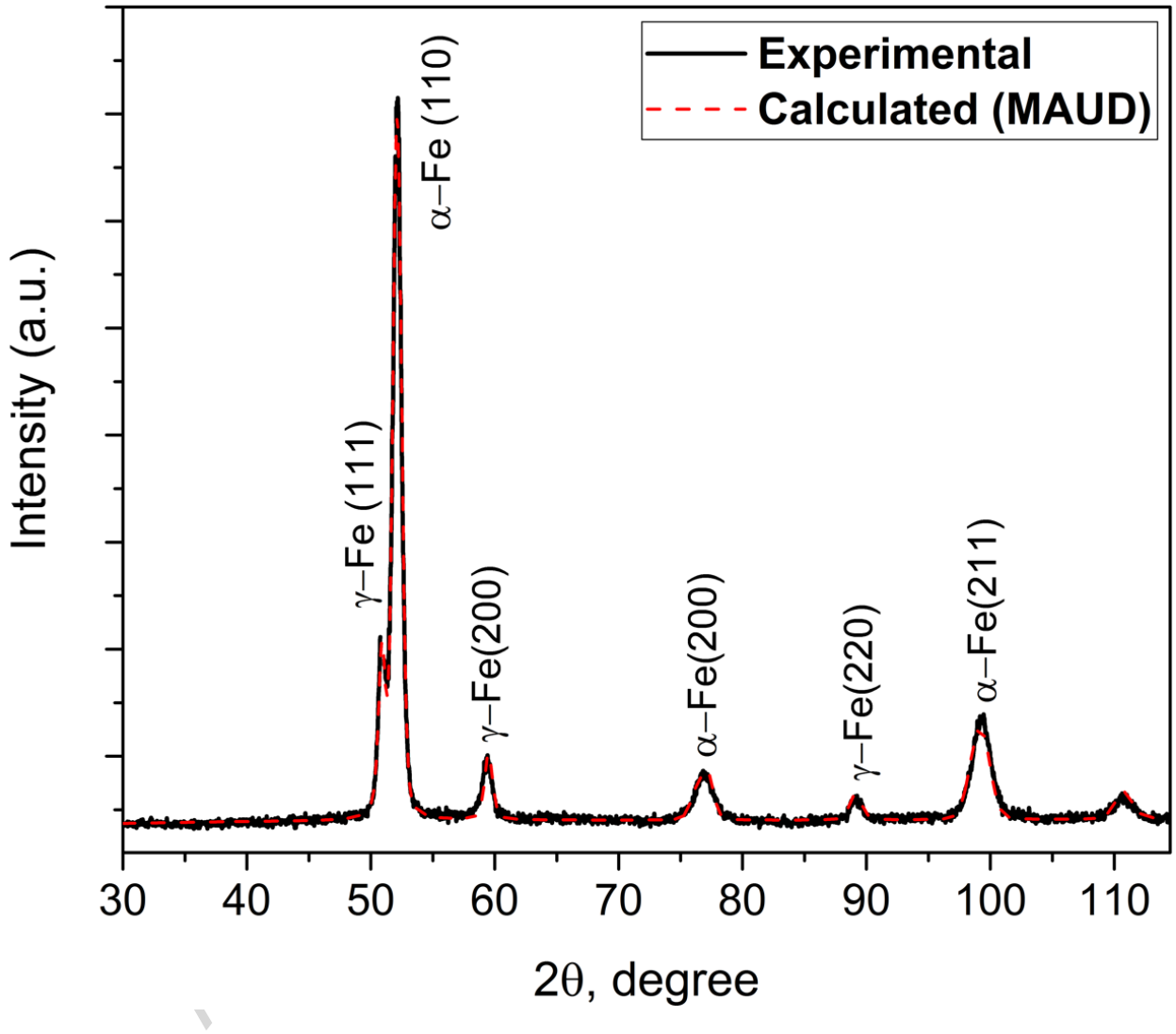

Figure 2

3.1.2 Composite Powders

The morphology and microstructure of the composite powders are depicted in Fig. 3. LMM flattened and fractured the H13 particles (Figs. 3a & b). A higher-magnification micrograph of the LMM powders (Fig.

3d) reveals signs of severe plastic deformation (please note the crescent-shaped area labeled A between the dashed curves) on the surface and in the near-surface areas of the H13 powder, where the cellular structure is deformed. Moreover, in the same figure, the distribution of PSZ nanoparticles, as indicated by the white arrow, seems to be very inhomogeneous, and PSZ particles are mainly concentrated on the surface of the matrix material, forming a shell-like structure. In view of the very high particle size ratio (d_{H13}/d_{PSZ}), the percolation threshold is apparently overcome by the very fine PSZ particles for both composites powders with 10 and 20 vol% PSZ reinforcements. These results are in line with those of a previous study of AlMangour et al.[16] and a mathematical model of the percolation threshold in a mixture of bimodal-sized soft and hard particles [28]. The average microhardness of the PSZ-added powders is slightly higher than that of AT-H13 (i.e., 720±43 HV0.05 vs. 690±10 HV0.05), which can be ascribed to local strain hardening on the particle surfaces and the inhomogeneous distribution of the reinforcing particles. The Cu Kα source, which is characterized by a limited penetration depth of several microns, was selected for the XRD analysis of LMM powders in order to obtain meaningful results on the extent of plastic deformation on the surface (Fig. 4a). The disappearance of peaks pertaining to γ-Fe confirms the strain induced γ–α transformation in the near-surface areas. Moreover, both the decrease in the mean crystallite size of α-Fe (i.e., 44± 6 nm vs. 75±5 nm) and the slight increase in the lattice microstrain from 0.3% to 0.4% indicate the effective plastic deformation on the surface.

In contrast, HMM resulted in a finer, more uniform particle size distribution (Fig. 3c) together with a much more refined microstructure consisting of UFG and nanocrystalline (NC) regions (Fig. 3e). Moreover, the dispersion of PSZ particles inside the matrix became more homogenous. Most particles were embedded in lamellas of severely deformed steel particles, in which the initial cellular network was destroyed. The number of PSZ particles remaining on the surface is very limited, which is further confirmed by the cross-sectional view of the polished and etched HMM particles in Fig. 3f, showing a severely deformed microstructure characterized by ultrafine lamellas and NC microstructure. The average microhardness of the HMM powders also increased to more than 1000 HV0.05, with a high standard deviation of 149 HV0.05 mainly due to the development of process-related micro- and nanoporosities, mainly at the conjunctions of cold-welded particles (white arrows in Figs. 3e & f)). The XRD spectra of the HMM particles is shown in Fig. 4b. The α-Fe mean crystallite size decreased to around 19±0.5 nm, while the increase in the lattice microstrain (i.e., 0.5%) confirms the presence of a high density of structural defects (e.g., dislocations) inside the HMM powders. Broadening of the peaks pertaining to t-ZrO_2 and c-ZrO_2 is indicative of a drastic decrease in mean crystallite size (i.e., nanocrystallization) of these phases due to the HMM. Moreover, introducing high levels of shear stresses enabled surpassing the percolation threshold of the fine PSZ particles and achieving a very homogenous distribution of PSZ in the severely deformed matrix.

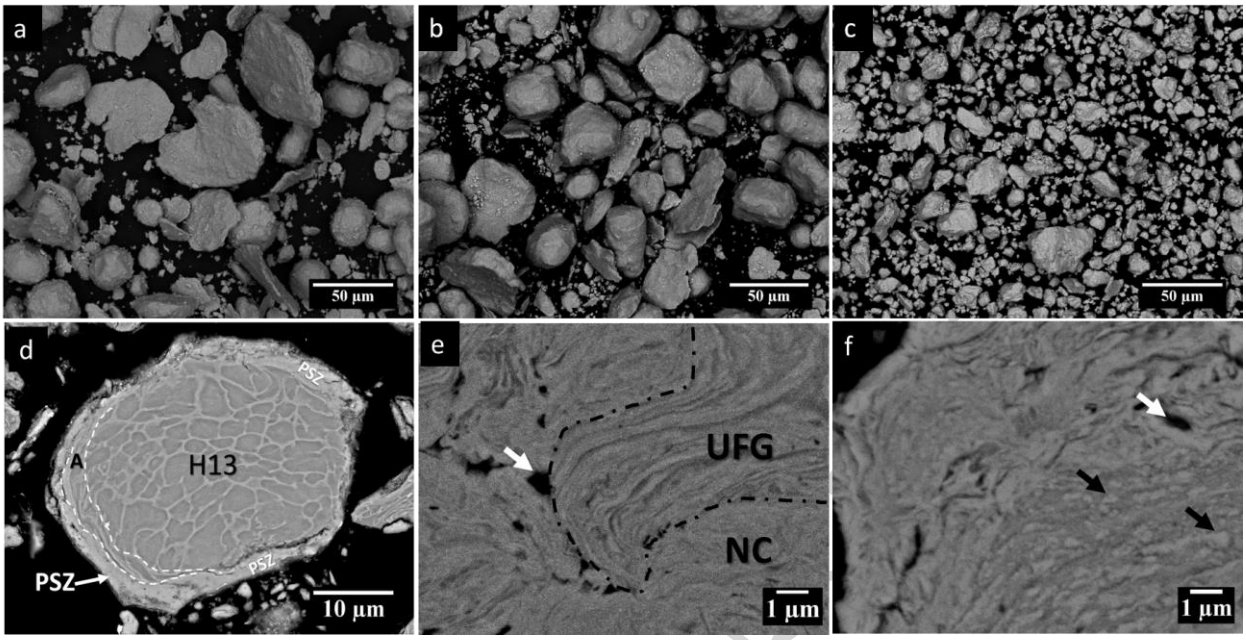

Figure 3. SEM micrographs of a) LMM (10%), b) LMM (20%), c) HMM (10%) composite powders; d) BSE cross-sectional micrographs of LMM (20%), e) HMM (10%), highlighting the UFG/NC structure after HMM, and d) HMM (10%), highlighting the dispersion of PSZ particles (brighter particles) inside the matrix

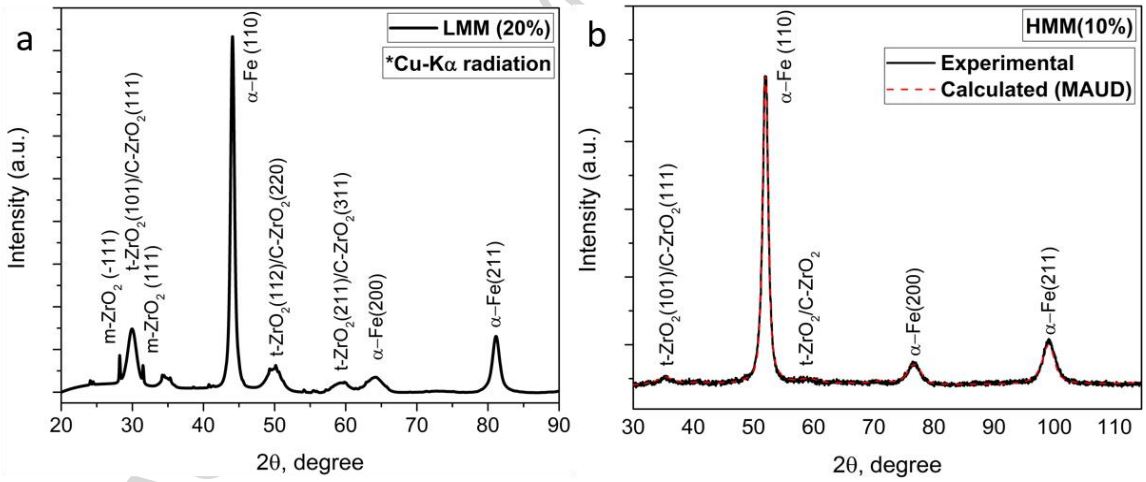

Figure 4. XRD patterns of a) LMM (20%) and b) HMM (10%) powders

3.2 Selective Laser Melting

3.2.1 Densification and defects in SLM-processed parts

For the purpose of comparison, the results of pure H13 samples are presented first. Figs. 5a and b depict the OM micrographs of AT-67 and AT-100 side views, respectively. The effect of the applied laser scanning speed, and therefore the energy density η, on the emergence of various laser-induced defects, namely, large pores due to incomplete densification and poor melting, small spherical pores, and hot cracking.

At $\eta = 67$ J/mm^3, the AT sample shows a relative density of 92.4%, exhibiting elongated pores as well as round pores with diameters on the scale of tens of microns (Fig. 5a). The large cavities formed at the track boundaries are attributed to the incomplete densification due to a short dwelling time (i.e., a low energy input) and the short penetration depth of the laser into the powder layer, leading to the incomplete melting of the particles (i.e., lack of fusion), which can be better appreciated in Fig. 5c. These powders can cause melt flow instability [29], [30], which negatively affects the wetting ability of the molten track resulting in formation of irregular pores between and along the boundaries [31]. The elongated pores at the layer boundaries are defined by a certain orientation with respect to the surface (see the side view of the SLM-processed part). These pores appear at the interlayer boundaries, which indicates that residual thermal stresses develop at the layer boundaries due to the repeated laser heating and subsequent fast cooling [32]. In general, substantial residual thermal stresses accumulate in SLM-processed parts during solidification due to the thermal shrinkage (i.e., strain) of the cooling molten top layer, which is opposed by the already-solidified bottom layers, resulting in residual stresses and subsequent thermal cracking. Therefore, microcracks due to tensile stresses are generally located between two adjacent layers.

At $\eta = 100$ J/mm^3, the parts show fewer large pores, and the relative density increases to the maximum of 96.1%. Compared with that in the parts processed at $\eta = 67$ J/mm^3, the metallurgical bonding between adjacent tracks is improved, and fewer large elongated pores are observed. However, at high energy inputs, the welding mechanism changes from conduction-mode welding to keyhole welding, meaning that in addition to melting the powder, the radiation energy is high enough to partially melt the already-processed layer below. This is also associated with the surface vaporization of the feedstock material, which generates gas bubbles that can remain trapped inside the melt pool during solidification [33]. The formation of such pores (indicated by white arrows in Fig. 5b) hinders the achievement of a near-full-density sample. Moreover, the number of fine microcracks at the layer boundaries was increased by increasing the energy density (indicated by black arrows in Fig. 5d), which is in line with the observations of Liu et al.[34], indicating that during the SLM of metallic materials, thermal shrinkage increases with the increasing energy density.

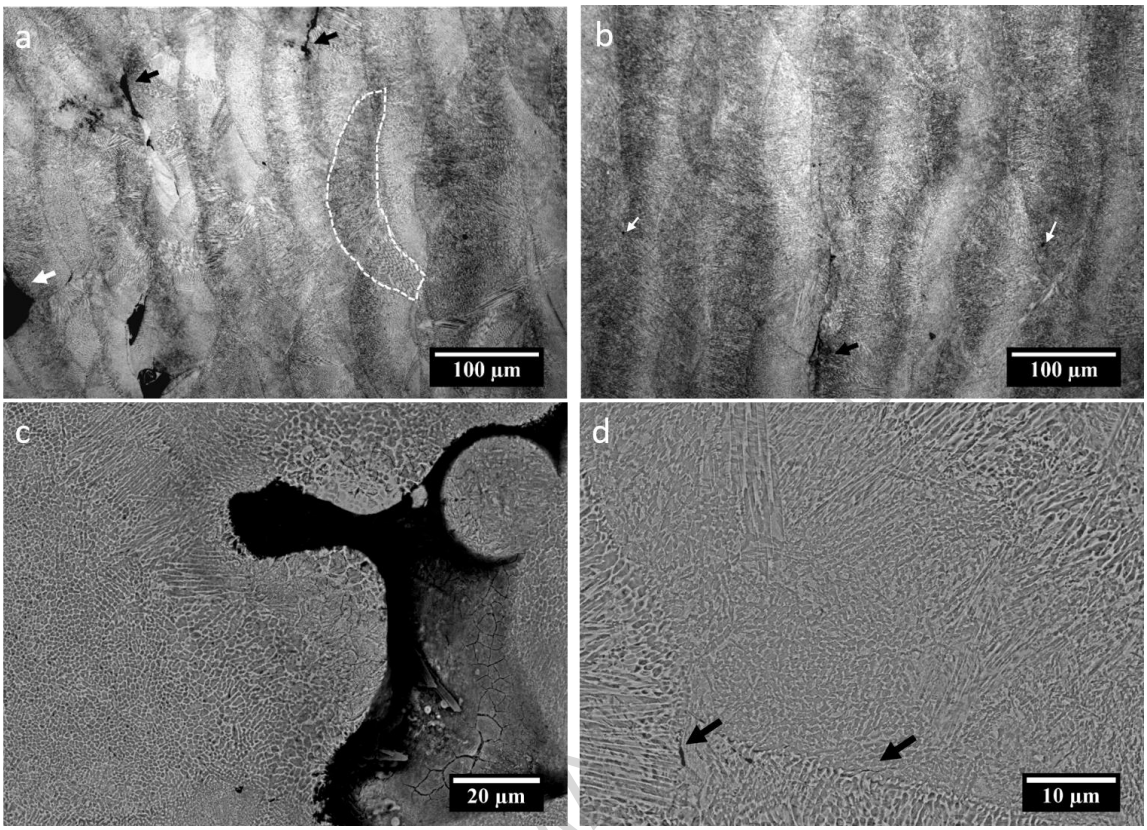

Figure 5. a) OM side-view micrographs of (a) AT-67, with the dashed area showing a track, and b) AT-100; SEM micrographs showing (c) poorly melted powders and large pores in AT-67 and d) microcracks at the layer boundary in AT-100

In addition to the aforementioned process-related defects, by introducing PSZ particles via LMM, "strings" of PSZ appeared mainly at the tracks and layers interface (Fig. 6a). These strings can be either attributed to the segregation of PSZ during solidification or the inhomogeneous dispersion of PSZ particles on the H13 powders surface, as discussed in section 3.1.2 and Fig. 3d. The formation mechanism of the segregated PSZ strings can be described in terms of the different material properties. Firstly, the temperature of the melt near the edges of the heat-affected zone (HAZ) is lower than that in the center of molten pool. Therefore, the material near the HAZ is denser than that in the center of molten pool. It is well known that the lower-temperature melt at the edge of the HAZ sinks in the molten pool due to the force of gravity (i.e., buoyancy force). Due to the different densities of the PSZ aggregates and H13 powders, they can be expected to move differently. Secondly, the role of surface tension should also be considered. The cooler material at the edge of the HAZ has a higher surface tension than the melt at the center of molten pool. Thus, the melt is pulled towards the edge of HAZ (Marangoni convection), since the heat conductivity of H13 is much higher than that of PSZ (i.e., 28.6 $Wm^{-1}K^{-1}$[35] vs. ~3 $Wm^{-1}K^{-1}$[36]). Therefore, the flow of these two materials will be different, resulting in the segregation of PSZ [37].

Most of the PSZ strings show internal cracking and debonding at the matrix/PSZ interface. Given that PSZ has a lower coefficient of thermal expansion (CTE) than the matrix, residual thermal stress is expected to develop at the H13/PSZ interface upon cooling from the processing temperature [38]. The stresses that arise from the CTE mismatch were theoretically calculated using Eshelby's equivalent inclusion theory [39] and experimentally investigated via XRD [22], [40], [41]. The stresses, which are hydrostatic in nature, are tensile in the H13 matrix but compressive in the PSZ due to PSZ's lower CTE. These stresses may overcome the interface strength, thus causing debonding of the interface. In addition, the tensile stresses in the matrix may also cause cracking in the adjacent PSZ agglomerates. Claussen [40] proposed a threshold agglomerate size, above which cracking may be observed, based on energy balance considerations, which can be expressed as follows:

$$d_c > C/\sigma_t \tag{5}$$

where d_c is the critical particle size, C is a constant depending on the matrix/reinforcement pair, and σ_t is the tensile stress. In many material combinations in which the reinforcing phase shows a lower CTE, relatively large particles can satisfy the abovementioned crack extension criterion. More importantly, it has been pointed that particle agglomerates (see Fig. 3d), in which the strain energy fields of individual particles may overlap each other, must be considered an equivalent large single particle [42]. Therefore, the PSZ agglomerates may have met the requirement in Eq. 3.

The segregated PSZ agglomerates were smaller in the HMM samples, and their morphology changed from large strings to isolated areas (Fig. 6b). Less cracking was observed inside the PSZ segregated regions, mainly because they were smaller size. Therefore, HMM can be beneficial in terms of improving the dispersion of PSZ inside the matrix, hence hindering excessive localized PSZ segregation and the formation of large PSZ strings. However, as discussed earlier, since the governing mechanisms of segregation in this system are highly dependent on the molten pool temperature, the segregation of PSZ seems to be inevitable. Therefore, the effect of energy density on the extent and morphology of segregated PSZ areas should also be studied in detail.

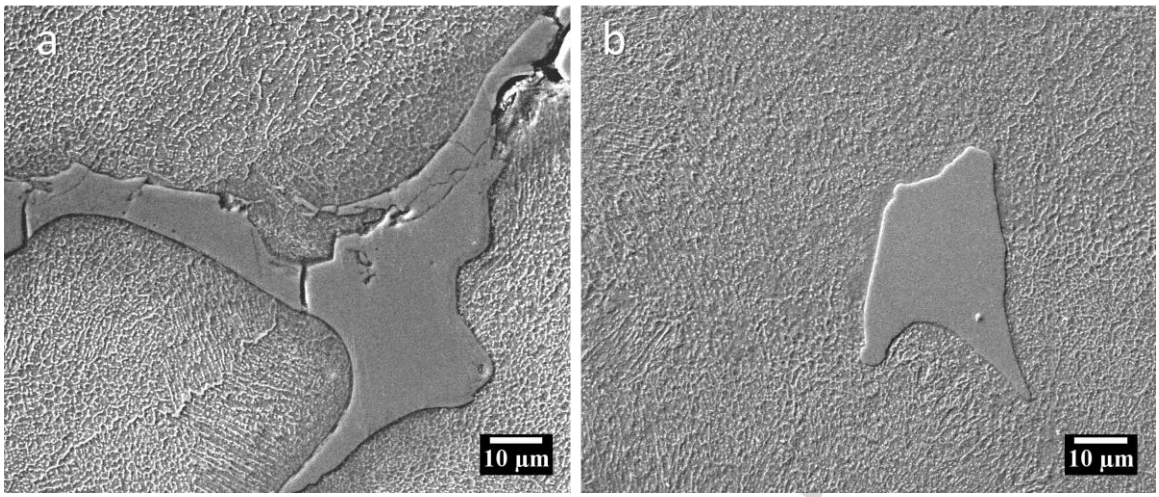

Figure 6 SEM micrographs showing the morphology and size of the PSZ reinforcements for a) LMM (10%)-67 and b) HMM (10%)-67

The density measurements in Table (3) confirm that HMM is advantageous in terms of improving the densification by decreasing the number and volume of segregated PSZ areas. Specifically, the relative densities of HMM (10%)-67 and HMM (10%)-100 (i.e., processed at $\eta = 67$ and 100) are 84.3% and 86.9%, respectively, which are slightly higher than those of the corresponding composites processed by LMM, i.e., LMM (10%)-67 and LMM (10%)-100, of 83.7% and 84.5%.

Table 3. Relative density of the samples

Sample	Relative density (%)
HMM (10%)-67	**84.3**
LMM (10%)-67	**83.7**
HMM (10%)-100	**86.9**
LMM (10%)-100	**84.5**
LMM (20%)-67	**82.9**
LMM (20%)-100	**80.2**
AT-67	**92.4**
AT-100	**96.5**

3.2.2 Microstructure and phases

Higher-magnification micrographs of the microstructure of the samples are shown in Fig. 7. All samples are characterized by cellular solidification, showing the microsegregation of the alloying elements at the cellular boundaries. Columnar grains with a high aspect ratio and equiaxed grains are observed. Equiaxed

grains have been reported to increase with the increasing build height because the influence of the heat flux decreases, and "competitive growth" becomes favored [32]. The PSZ particles (excluding the segregated PSZ areas) seem to be homogenously dispersed in the matrix. In view of the higher melting temperature of PSZ (T_m~2680°C), PSZ particles may be partially melted. Thus nucleation of PSZ and subsequent grain growth are expected to occur first However, as the solidification is very rapid in SLM, reaching rates as high as 10^3–10^7 K s^{-1}[11], growth of PSZ nuclei is highly restricted because of the inadequate time; therefore, most of the PSZ particles remain nano-sized. The number of fine oxide particles is increased in the HMM SLM-processed parts (dark spots in Fig. 7d). During HMM, oxygen is taken up due to the increased temperature and smaller particles of highly reactive steel powders. The oxygen content was measured to be one order of magnitude higher in MM H13 particles relative to that in the starting AT powder [43]. Therefore, it can be concluded that the higher amount of dispersed oxides is a consequence of HMM. Moreover, signs of microsegregation of PSZ (indicated by the dashed circle in Fig. 8) at the prior cellular boundaries are shown in a higher-magnification micrograph. This microsegregation has previously been reported for other SLM-processed MMCs [44]. The existence of Marangoni convection within the pool pushes several nucleated PSZ particles towards the cell boundaries during solidification of H13, forming a very fine ring of PSZ particles near the cell boundaries.

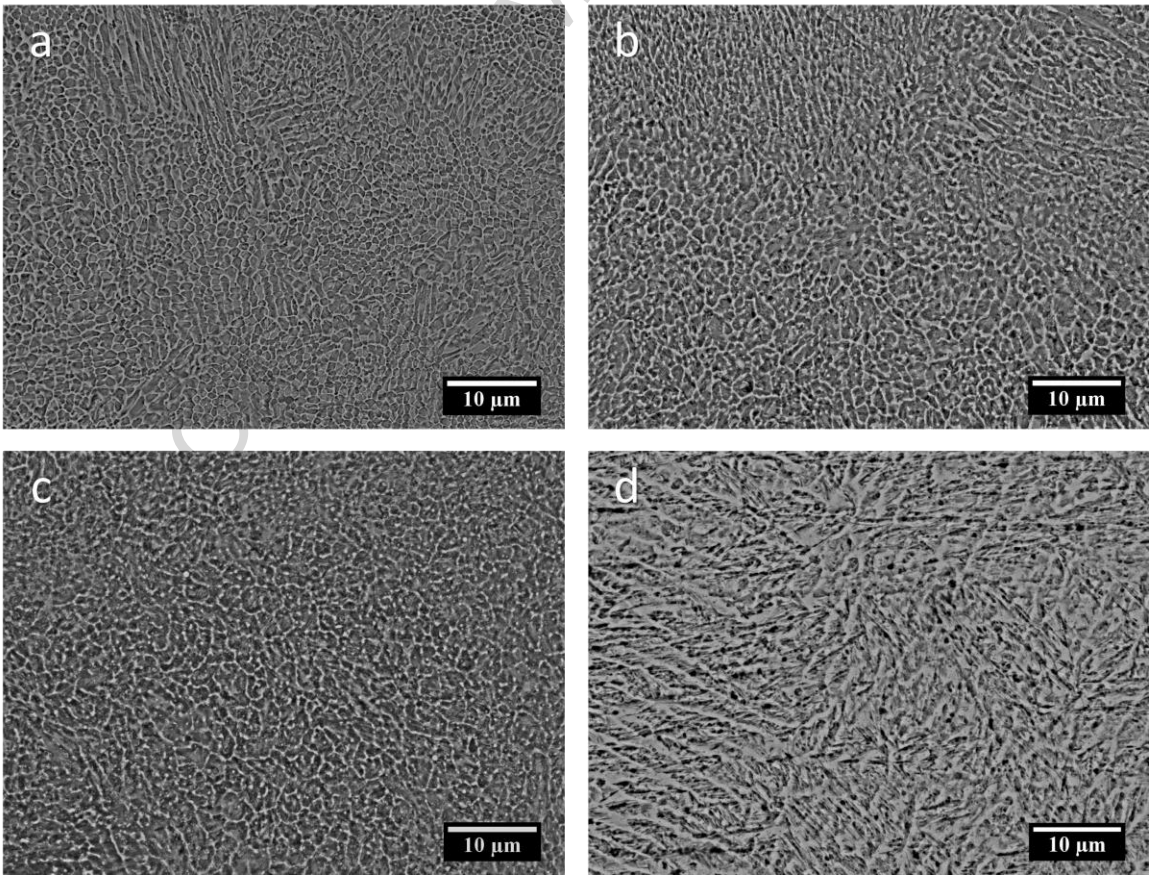

Figure 7.BSE side-view micrographs of a) AT-100, b) LMM (10%)-100, c) LMM (20%)-100 and d) HMM (10%)-100, in which brighter particles are PSZ

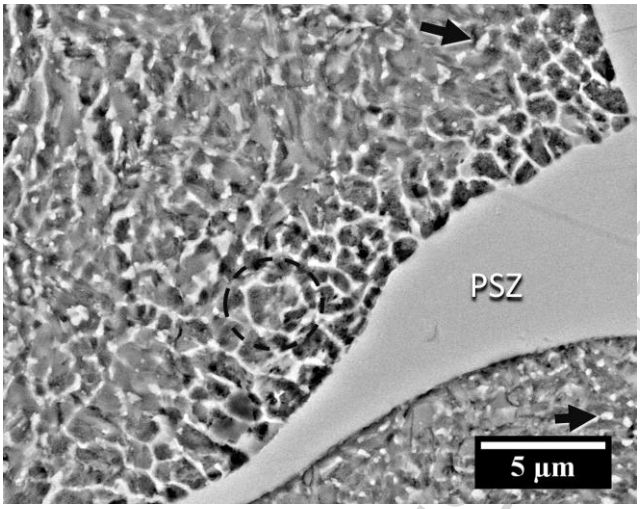

Figure 8. BSE micrograph showing microsegregation of PSZ inside the matrix in the vicinity of a segregated PSZ string. The dashed circle indicates the microsegregation of PSZ in a ring form at the cell boundaries, and the black arrows point to dispersed PSZ particles

The XRD spectra and quantitative phase analysis results of the samples shown in Fig. 9 and Table 4, respectively, demonstrate that the AT samples mostly consists of martensite and RA.

During the SLM processing of H13, the powders melt and then solidify at a very high cooling rate down to temperatures below the martensite start temperature (M_s), thus forming a microstructure composed of only martensite and austenite. In fact, any carbide precipitation is suppressed by the rapid cooling, giving rise to very stable austenite (low M_s) containing the maximum possible amount of alloying elements. For the purpose of comparison, it is worth mentioning that H13 quenched from 1020–1040°C, at which undissolved carbides are still present, shows up to only 2–4% RA. During melting of the overlying deposited powder layer, the heat transfer (the heat flow direction is normal to the build platform) from the overlying layer may increase the temperature of the already-solidified layer directly under the molten pool above the Ac_1 temperature (i.e., the temperature at which austenite begins to form during heating). Therefore, the martensite will retransform into austenite, which will be quenched again below M_s to form martensite. On the other hand, the portion of the material reheated up to $T<Ac_1$ undergoes tempering, as confirmed by darker areas (Figs. 5a-b). These darker areas can be ascribed to the higher reactivity to chemical etching due to secondary carbide precipitation.

Nevertheless, the high amount of RA in the SLM samples is also correlated to the chemical stabilization of austenite due to intercellular microsegregation (Fig. 7). A similar effect was previously described for

SLM-processed maraging steel containing up to 8.5% austenite in the as-built condition. The same steel produced by the conventional route (i.e., ingot casting and forging) does not contain any RA due to the high chemical homogeneity of the material [45]. Finally, it has been proposed that RA can be stabilized by the diffusion of C from supersaturated martensite [46]. The volume percentage of RA in AT-67, in which the energy density is relatively low, is lower than that of AT-100 (i.e., 13 vol% vs. 17 vol%, respectively), which confirms the influence of heat flow on the formation and stabilization of RA. Although this difference in RA is not very significant, it can be most plausibly explained by the more severe microsegregation in the case of the lower deposition energy. The mean crystallite size of α-Fe is 29±1.5 nm in the case of $\eta = 67$ J/mm^3, while it becomes 41±1 nm at $\eta = 100$ J/mm^3. The most probable explanation is that more heat accumulates as a result of the elevated energy density, leading to grain coarsening by providing a higher internal energy. The lattice microstrain in the AT-67 and AT-100 samples was calculated to be around 0.25% and 0.2%, respectively, indicative of a relatively high density of structural defects in the microstructure.

In case of the composites, the main feature revealed by XRD analysis is the large volume fraction of t-ZrO_2, which is essential to improving the mechanical properties of the H13–PSZ composites. In addition, these composites exhibit less RA (Table 4), which can explain another feature of the composites. The decreased RA content in steel matrix composites is reported to be due to hydrostatic residual thermal tensile stresses in the matrix, which developed upon cooling from the processing temperature. Stresses applied to the parent phase (i.e., the high-temperature austenite) can induce martensitic transformation in iron alloy systems [47]. The work of Patel and Cohen [48] confirms that displacive shear-like martensitic transformation can be achieved by applying external tensile or compressive stresses. These external stresses, if applied at temperatures above the M_S (i.e., the temperature at which the transformation occurs spontaneously upon cooling) may activate the transformation, thus increasing the M_S due to a decrease in the chemical driving force for the martensitic transformation ($\Delta F^{\gamma-\alpha}$), which decreases the critical strain energy for martensite transformation ($\Delta G_i^{\gamma-\alpha}$). As mentioned in section 3.2.1, internal residual thermal stresses can develop in composites (i.e., tensile stresses in H13 matrix and compressive stresses in the PSZ reinforcement) during cooling due to the presence of PSZ particles. Therefore, a higher volume percent of martensite can be achieved in composite. These observations are in line with the work of Pagounis et al. [49] on the effect of CTE mismatch on the martensitic transformation in steel matrix composites. The EDS analysis results presented in the next section also confirm the limited reaction of PSZ with the H13 matrix, which produces complex oxides containing Cr, V, and Si. Moreover, preliminary thermodynamic simulations suggest that ZrC and silicates form upon cooling the composite

from the processing temperature. Therefore, the depletion of C from the H13 matrix may have contributed to a change in the *Ms* of the matrix material, thus leading to less RA in the final matrix material.

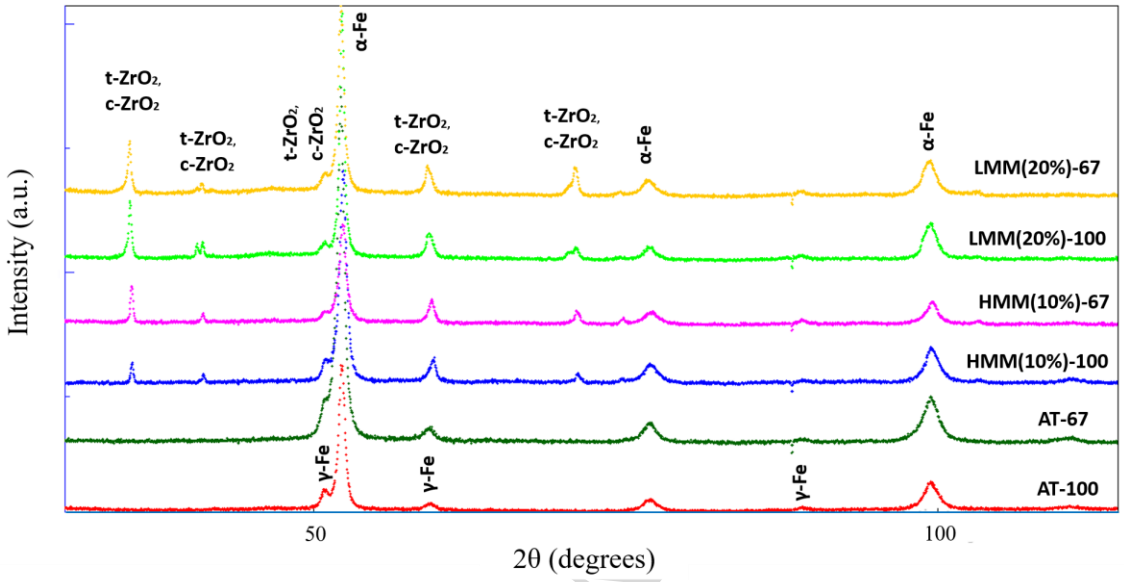

Figure 9. XRD patterns of the SLM-processed samples

Table 4. XRD quantitave phase analysis results of SLM-processed samples

Sample label	α-Fe (vol%)	γ-Fe (vol%)	t+c ZrO_2 (vol%)	m-ZrO_2 (vol%)
HMM (10%)-67	**86**	**7**	**6**	**<1**
HMM (10%)-100	**85**	**9**	**5**	**<1**
LMM (20%)-67	**81**	**5**	**12**	**<2**
LMM (20%)-100	**79**	**6**	**13**	**<2**
AT-67	**87**	**13**	**-**	**-**
AT-100	**83**	**17**	**-**	**-**

3.2.3 Matrix/reinforcement interface

Although the XRD analysis did not reveal any unexpected reaction phases in composites, the SEM micrographs of H13/PSZ interface together with the EDS line scan analysis (Fig. 10) indicate that the interface is characterized by a very thin reaction layer (less than 5 μm) with high concentrations of Cr and V. Chemical reactions between the H13 and the PSZ particles may also affect the mechanical properties of the composites. In general, the coexistence of Cr_2O_3 and ZrO_2 at the steel/zirconia joint is

thermodynamically plausible at high temperatures (1300°C) and an oxygen partial pressure greater than 5.7×10^{-10} mbar [25]. Under these conditions, ZrO_2 can be reduced at the expense of oxidizing Cr. However, Zr does not completely reduce, and zirconia exists in a non-stoichiometric state, as expressed by the following equation [50]:

$$ZrO_2 \rightarrow ZrO_{2-X} + X/2O_2\,, \qquad 0 \leq X \leq 0.02 \tag{4}$$

Thus, the reaction kinetics probably allow the formation of a reaction zone in the composites. These complex oxides may negatively influence the mechanical properties of the composites.

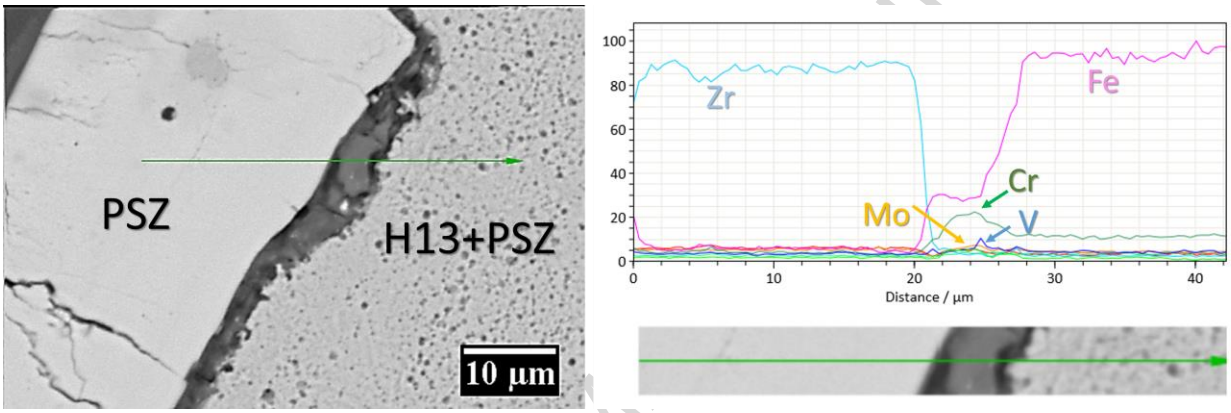

Figure 10. (Left) SEM micrograph showing the line scan analysis position and (right) the corresponding EDS line scan elemental analysis results

3.2.4 Microstructure and phases in quenched condition

As depicted in Fig. 11, THE XRD analysis of the quenched AT samples confirms the achievement of a fully martensitic microstructure. In the case of composites, the presence of tetragonal and cubic zirconia is also evident.

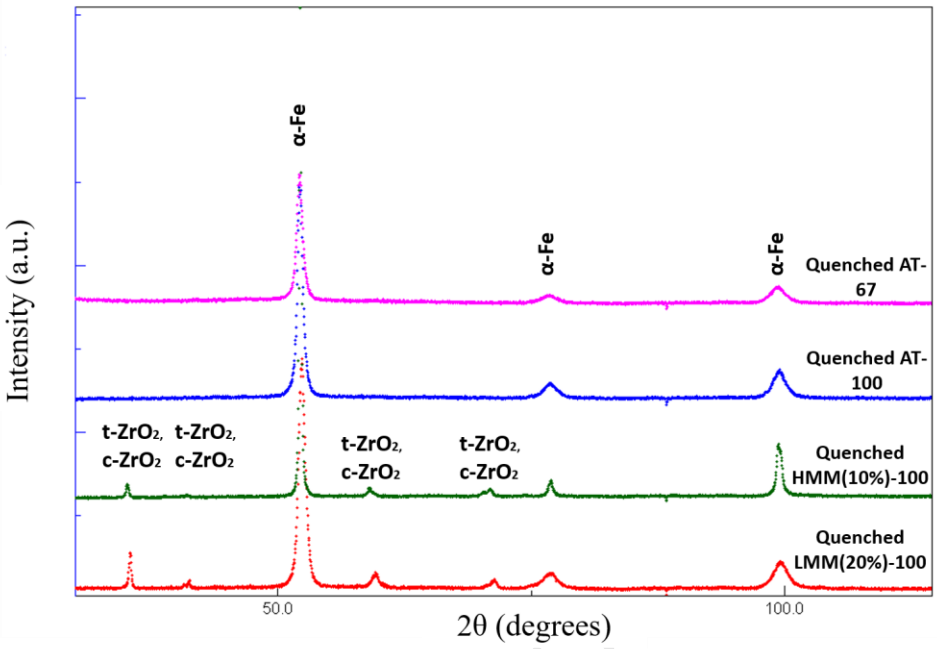

Figure 11. XRD patterns of SLM-processed quenched AT samples and composites

Figs. 12a & b imply that the austenitizing quenching treatment forms fine equiaxed grains. The presence of finely dispersed PSZ particles is more obvious in the quenched composites (Figs. 12 c & d). The nanosized PSZ particles show two different morphologies (i.e., spherical and irregular). The spherical particles are most likely formed from the microsegregated PSZ (see Fig. 8) at the prior austenite boundaries during austenitization and quenching. At 1020°C (i.e., the austenitization temperature in this work), the microsegregated PSZs tend to decrease their free surface energy by becoming spheroidized, similar to non-dissolved carbides spheroidizing during the high-temperature annealing of tool steels.

The irregular PSZ nanoparticles are actually those that were successfully dispersed in the matrix (i.e., isolated fine particles) during MM. At least some of these particles may have appeared in the supersaturated matrix due to the non-equilibrium solidification during SLM, eventually re-precipitating during heating to the austenitization temperature, at which point the material is more approaching towards the equilibrium conditions [51]. However, according to the literature [51], [52], this implies the dissociation of ZrO_2 and the presence of Zr in the metastable supersaturated matrix (i.e., α-Fe(Zr)) followed by subsequent precipitation in the solidified matrix either during SLM or the thermal post processing. In this condition, the final compound is not always ZrO_2 but nanoparticles of other compounds (e.g., Fe_2Zr and ZrC) [53], [54]. Since the XRD patterns do not indicate the presence of large volumes of newly formed phases, even though this may occur during SLM processing, another possible scenario would be that isolated un-dissolved solid PSZ particles are trapped by the solid–liquid interface

during solidification. This explanation seems plausible considering that the irregularly shaped particles range in size from 0.5 to 2 μm, roughly corresponding to the average particle size of the starting PSZ. This explanation may also explain the different PSZ particle morphologies in the composites. However, the effects of composition and microstructural evolution either during SLM or the post thermal treatment stage should be further elaborated in future studies to confirm this hypothesis.

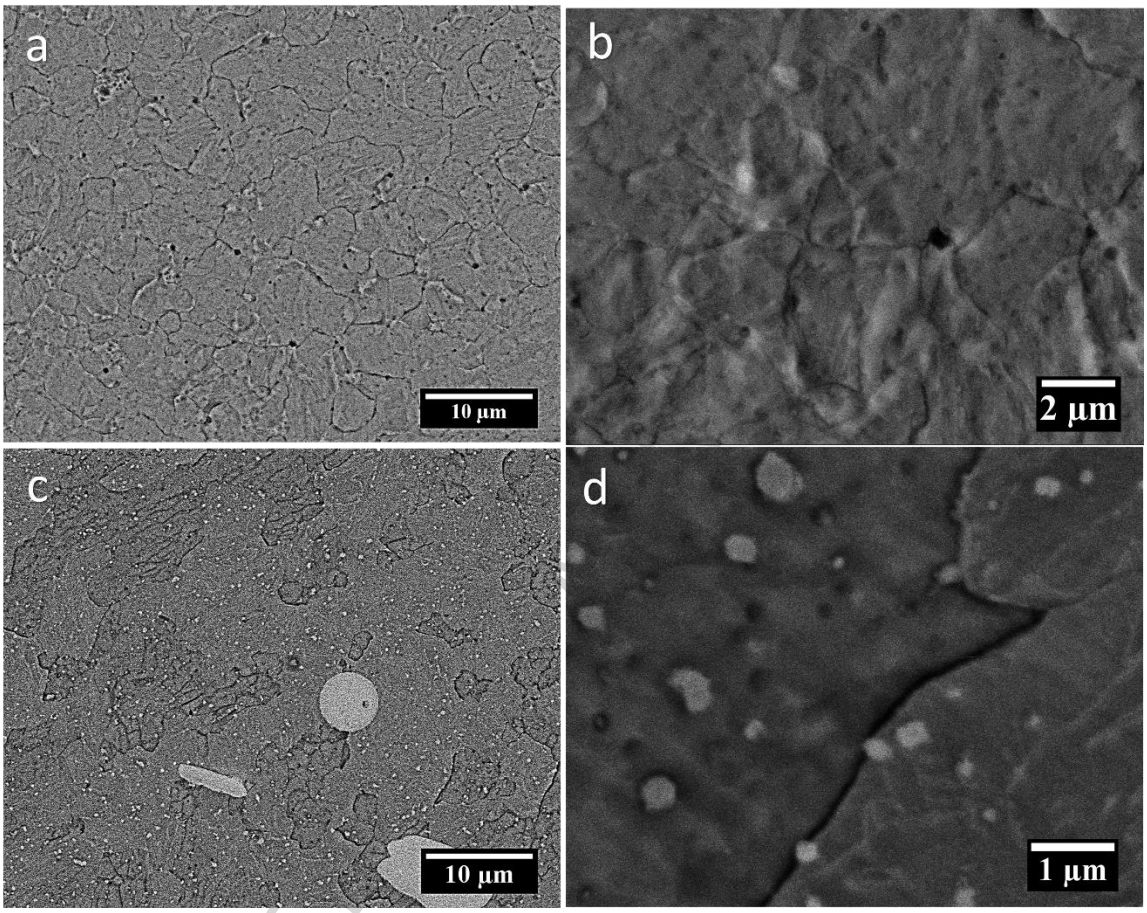

Figure 12. Side-view SEM micrographs of quenched samples. a) BSE micrograph of AT-67, b) higher-magnification back-scattered electrons (BSE) micrograph highlighting the grain morphology, c) BSE micrograph of HMM(10%)-67 and d) higher-magnification BSE micrograph of HMM(10%)-67

3.2.5 Microhardness measurements

The microhardness results of the SLM-processed parts are shown in Fig. 13. The microhardness of AT-100 is higher than that of AT-67, mainly because of its higher relative density. The microhardness of the composites was higher than that of the matrix material and generally increased with the increasing energy density, mainly because this increases the relative density of the material. The contributions of the PSZ particles (i.e., dispersion hardening and grain boundary pinning) increase the microhardness, and a

maximum microhardness of 800 HV0.1 is achieved by incorporating 20 vol% PSZ at an energy density of 100 J/mm^3. In these composites, the dispersion hardening effect is negatively affected by the increased porosity. However, the microhardness can be further increased to around 900 HV0.1 by using HMM and only 10 vol% PSZ. The significantly improved microhardness can be attributed to the i) finer, more homogenous dispersion of PSZ particles due to the HMM, ii) higher relative density, and iii) contribution of non-metallic oxides as secondary hard particles inside the HMM composite powders. In view of the significantly increased hardness of the HMM samples, the samples will be observed with transmission electron microscopy in the future to obtain meaningful data on the distribution and size of the nanoparticles (both non-metallic oxides and PSZ particles). These observations will enable estimating and individuating the particle strengthening contributions of these particles in SLM-processed tool steel composites reinforced with PSZ and processed with different MA energies and SLM processing parameters.

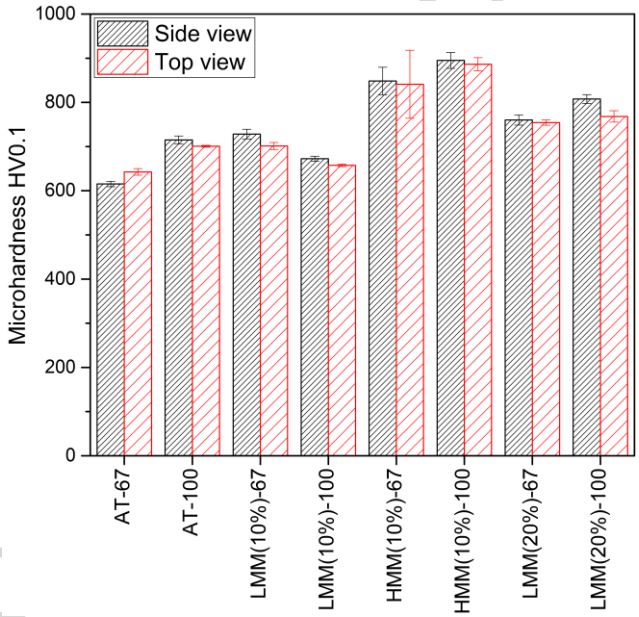

Figure 13. Microhardness measurement results

4. Conclusions

The analysis of the densification behavior, microstructure, and phase constitution of SLM-processed H13–PSZ composite powders showed that the proposed processing route is suitable for the production of such MMCs. However, the process should be further optimized to obtain higher relative densities and samples free from thermal cracking. The main conclusions are as follows:

- Due to the high particle size ratio (d_{H13}/d_{PSZ}) and the presence of 10 and 20 vol% PSZ, the percolation threshold was overcome in powders mixtures. Therefore, HMM was necessary to homogenously disperse the reinforcing particles inside the severely deformed matrix and to bypass this threshold. This could not be achieved by LMM.
- At η = 67 J/mm^3, the powders were poorly melted, resulting in incomplete densification. Increasing the energy density to 100 J/mm^3 resulted in maximum densification; however, spherical pores and thermal cracking were observed due to the longer lifetime of the liquid in the molten pool and high thermal stresses.
- The high amount of RA in SLM samples can mainly be attributed to the chemical stabilization of austenite because of the intercellular microsegregation.
- Some PSZ particles (agglomerates) were highly segregated in the SLM-processed composites due to variations in the movement of PSZ particles within the molten pool because of the buoyancy and Marangoni effects. HMM was beneficial because it provided a homogenous dispersion of PSZ inside the matrix, thus hindering excessive localized PSZ segregation and the formation of large PSZ segregated areas. However, since the segregation phenomenon is mostly related to the material properties and SLM processing parameters, the effects of the SLM energy density on the extent and morphology of segregated PSZ should be studied in detail.
- Traces of a limited interfacial reaction in the H13–PSZ composites were found by an EDS line scan analysis. The reaction layer was characterized by the co-existence of complex oxides. However, these oxides were not detected by the XRD analysis, indicating their small volume fraction in the composite.
- The as-built and quenched composites showed a large amount of metastable t-ZrO_2. Therefore, the transformation toughening effect of PSZ can be exploited to achieve a higher fracture toughness in these composites. Considering their use in critical applications where premature or catastrophic failure is unacceptable, an important prerequisite for these composites is an acceptable level of fracture toughness. Thus, the present results suggest that increasing the relative density of the composites is important to optimize the mechanical properties.
- The microhardness of the composites was generally higher than that of the base material. HMM SLM-processed parts showed a maximum microhardness of around 900 $HV_{0.1}$ due to the i) more homogenous dispersion of PSZ particles (i.e., dispersion hardening), ii) slightly higher relative density than that of their LMM SLM-processed counterparts and iii) oxygen pick-up during the HMM (i.e., the formation of dispersed oxides contributes to strengthening).

References

[1] "Tool Steels, 5th Edition - ASM International." [Online]. Available: http://www.asminternational.org/search/-/journal_content/56/10192/06590G/PUBLICATION. [Accessed: 14-Dec-2016].

[2] F. Nair and M. B. Karamis, "An investigation of the tribological interaction between die damage and billet deformation during MMC extrusion," *Tribol. Int.*, vol. 43, no. 1–2, pp. 347–355, Jan. 2010.

[3] H. Berns, "Comparison of wear resistant MMC and white cast iron," *Wear*, vol. 254, no. 1–2, pp. 47–54, Jan. 2003.

[4] E. Pagounis, M. Talvitie, and V. K. Lindroos, "Microstructure and Mechanical Properties of Hot Work Tool Steel Matrix Composites Produced by Hot Isostatic Pressing," *Powder Metall.*, vol. 40, no. 1, pp. 55–61, Jan. 1997.

[5] N. Chawla and Y.-L. Shen, "Mechanical Behavior of Particle Reinforced Metal Matrix Composites," *Adv. Eng. Mater.*, vol. 3, no. 6, pp. 357–370, Jun. 2001.

[6] E. Pagounis and V. K. Lindroos, "Processing and properties of particulate reinforced steel matrix composites," *Mater. Sci. Eng. A*, vol. 246, no. 1–2, pp. 221–234, May 1998.

[7] D. H. Bacon, L. Edwards, J. E. Moffatt, and M. E. Fitzpatrick, "Fatigue and fracture of a 316 stainless steel metal matrix composite reinforced with 25% titanium diboride," *Int. J. Fatigue*, vol. 48, pp. 39–47, Mar. 2013.

[8] R. C. Garvie, R. H. Hannink, and R. T. Pascoe, "Ceramic steel?," *Nature*, vol. 258, no. 5537, pp. 703–704, Dec. 1975.

[9] R. H. J. Hannink, P. M. Kelly, and B. C. Muddle, "Transformation Toughening in Zirconia-Containing Ceramics," *J. Am. Ceram. Soc.*, vol. 83, no. 3, pp. 461–487, Mar. 2000.

[10] R. M. McMeeking, "Effective Transformation Strain in Binary Elastic Composites," *J. Am. Ceram. Soc.*, vol. 69, no. 12, p. C-301, Dec. 1986.

[11] D. D. Gu, W. Meiners, K. Wissenbach, and R. Poprawe, "Laser additive manufacturing of metallic components: materials, processes and mechanisms," *Int. Mater. Rev.*, vol. 57, no. 3, pp. 133–164, May 2012.

[12] W. Meiners, C. Over, K. Wissenbach, and R. Poprawe, *Direct Generation of Metal Parts and Tools by Selective Laser Powder*. .

[13] M. J. Holzweissig, A. Taube, F. Brenne, M. Schaper, and T. Niendorf, "Microstructural Characterization and Mechanical Performance of Hot Work Tool Steel Processed by Selective Laser Melting," *Metall. Mater. Trans. B*, vol. 46, no. 2, pp. 545–549, Apr. 2015.

[14] C. S. Wright, M. Youseffi, S. P. Akhtar, T. H. C. Childs, C. Hauser, and P. Fox, "Selective Laser Melting of Prealloyed High Alloy Steel Powder Beds," *Mater. Sci. Forum*, vol. 514–516, pp. 516–523, 2006.

[15] F. Klocke, K. Arntz, M. Teli, K. Winands, M. Wegener, and S. Oliari, "State-of-the-art Laser Additive Manufacturing for Hot-work Tool Steels," *Procedia CIRP*, vol. 63, pp. 58–63, Jan. 2017.

[16] B. AlMangour, D. Grzesiak, and J.-M. Yang, "Nanocrystalline TiC-reinforced H13 steel matrix nanocomposites fabricated by selective laser melting," *Mater. Des.*, vol. 96, pp. 150–161, Apr. 2016.

[17] M. J. Tan and X. Zhang, "Powder metal matrix composites: selection and processing," *Mater. Sci. Eng. A*, vol. 244, no. 1, pp. 80–85, Mar. 1998.

[18] I. Sabirov, O. Kolednik, R. Z. Valiev, and R. Pippan, "Equal channel angular pressing of metal matrix composites: Effect on particle distribution and fracture toughness," *Acta Mater.*, vol. 53, no. 18, pp. 4919–4930, Oct. 2005.

[19] F. Y. C. Boey, Z. Yuan, and K. A. Khor, "Mechanical alloying for the effective dispersion of sub-micron SiCp reinforcements in Al–Li alloy composite," *Mater. Sci. Eng. A*, vol. 252, no. 2, pp. 276–287, Sep. 1998.

[20] C. Suryanarayana, "Mechanical alloying and milling," *Prog. Mater. Sci.*, vol. 46, no. 1–2, pp. 1–184, Jan. 2001.

[21] J. Williams, D. Miller, and C. Deckard, "Selective Laser Sintering Part Strength as Function of Andrew Number, Scan Rate and Spot Size," in *Proceedings of Solid Freeform Fabrication Symposium 1996*, 1996, pp. 549–557.

[22] F. Deirmina and M. Pellizzari, "Production and characterization of a tool steel-PSZ composite by mechanical alloying and spark plasma sintering," *J. Alloys Compd.*, vol. 709, pp. 742–751, Jun. 2017.

[23] L. Lutterotti, S. Matthies, H.-R. Wenk, A. S. Schultz, and J. W. R. Jr, "Combined texture and structure analysis of deformed limestone from time-of-flight neutron diffraction spectra," *J. Appl. Phys.*, vol. 81, no. 2, pp. 594–600, Jan. 1997.

[24] M. F. Ashby and Y. J. M. Bréchet, "Designing hybrid materials," *Acta Mater.*, vol. 51, no. 19, pp. 5801–5821, Nov. 2003.

[25] M. Dourandish, A. Simchi, E. Tamjid Shabestary, and T. Hartwig, "Pressureless Sintering of 3Y-TZP/Stainless-Steel Composite Layers," *J. Am. Ceram. Soc.*, vol. 91, no. 11, pp. 3493–3503, Nov. 2008.

[26] C. McVeigh, F. Vernerey, W. K. Liu, B. Moran, and G. Olson, "An interactive micro-void shear localization mechanism in high strength steels," *J. Mech. Phys. Solids*, vol. 55, no. 2, pp. 225–244, Feb. 2007.
[27] A. Lawley, "Atomization of Specialty Alloy Powders," *JOM*, vol. 33, no. 1, pp. 13–18, Jan. 1981.
[28] D. Bouvard, "Densification behaviour of mixtures of hard and soft powders under pressure," *Powder Technol.*, vol. 111, no. 3, pp. 231–239, Sep. 2000.
[29] C. Qiu, N. J. E. Adkins, and M. M. Attallah, "Selective laser melting of Invar 36: Microstructure and properties," *Acta Mater.*, vol. 103, no. Supplement C, pp. 382–395, Jan. 2016.
[30] D. Gu *et al.*, "Densification behavior, microstructure evolution, and wear performance of selective laser melting processed commercially pure titanium," *Acta Mater.*, vol. 60, no. 9, pp. 3849–3860, May 2012.
[31] R. Li, Y. Shi, Z. Wang, L. Wang, J. Liu, and W. Jiang, "Densification behavior of gas and water atomized 316L stainless steel powder during selective laser melting," *Appl. Surf. Sci.*, vol. 256, no. 13, pp. 4350–4356, Apr. 2010.
[32] N. J. Harrison, I. Todd, and K. Mumtaz, "Reduction of micro-cracking in nickel superalloys processed by Selective Laser Melting: A fundamental alloy design approach," *Acta Mater.*, vol. 94, no. Supplement C, pp. 59–68, Aug. 2015.
[33] M. Garibaldi, I. Ashcroft, M. Simonelli, and R. Hague, "Metallurgy of high-silicon steel parts produced using Selective Laser Melting," *Acta Mater.*, vol. 110, no. Supplement C, pp. 207–216, May 2016.
[34] Y. Liu, Y. Yang, and D. Wang, "A study on the residual stress during selective laser melting (SLM) of metallic powder," *Int. J. Adv. Manuf. Technol.*, vol. 87, no. 1–4, pp. 647–656, Oct. 2016.
[35] K.-A. Chiang and Y.-C. Chen, "Laser surface hardening of H13 steel in the melt case," *Mater. Lett.*, vol. 59, no. 14, pp. 1919–1923, Jun. 2005.
[36] K. W. Schlichting, N. P. Padture, and P. G. Klemens, "Thermal conductivity of dense and porous yttria-stabilized zirconia," *J. Mater. Sci.*, vol. 36, no. 12, pp. 3003–3010, Jun. 2001.
[37] K. A. Mumtaz and N. Hopkinson, "Laser melting functionally graded composition of Waspaloy<Superscript>®</Superscript> and Zirconia powders," *J. Mater. Sci.*, vol. 42, no. 18, pp. 7647–7656, Sep. 2007.
[38] E. Pagounis and V. K. Lindroos, "The role of internal stresses on the phase transformation of iron alloys," *Scr. Mater.*, vol. 37, no. 1, pp. 65–69, Jul. 1997.
[39] P. J. Withers, W. M. Stobbs, and O. B. Pedersen, "The application of the eshelby method of internal stress determination to short fibre metal matrix composites," *Acta Metall.*, vol. 37, no. 11, pp. 3061–3084, Nov. 1989.
[40] M. Ceretti, C. Braham, J. l. Lebrun, J. p. Bonnafe, M. Perrin, and A. Lodini, "Residual Stress Analysis by Neutron and X-Ray Diffraction Applied to the Study of Two Phase Materials: Metal Matrix Composites," *Exp. Tech.*, vol. 20, no. 3, pp. 14–18, May 1996.
[41] S.-D. Tsai, D. Mahulikar, H. L. Marcus, I. C. Noyan, and J. B. Cohen, "Residual stress measurements on Al-graphite composites using X-ray diffraction," *Mater. Sci. Eng.*, vol. 47, no. 2, pp. 145–149, Feb. 1981.
[42] F. F. Lange, "Effect of Microstructure on Strength of Si3N4-SiC Composite System," *J. Am. Ceram. Soc.*, vol. 56, no. 9, pp. 445–450, Sep. 1973.
[43] A. Fedrizzi, "Production of steel matrix composites by mechanical milling and spark plasma sintering," phd, University of Trento, 2013.
[44] D. Gu, H. Wang, D. Dai, P. Yuan, W. Meiners, and R. Poprawe, "Rapid fabrication of Al-based bulk-form nanocomposites with novel reinforcement and enhanced performance by selective laser melting," *Scr. Mater.*, vol. 96, pp. 25–28, Feb. 2015.
[45] E. A. Jägle, Z. Sheng, P. Kürnsteiner, S. Ocylok, A. Weisheit, and D. Raabe, "Comparison of Maraging Steel Micro- and Nanostructure Produced Conventionally and by Laser Additive Manufacturing," *Materials*, vol. 10, no. 1, Dec. 2016.
[46] M. J. Holzweissig, A. Taube, F. Brenne, M. Schaper, and T. Niendorf, "Microstructural Characterization and Mechanical Performance of Hot Work Tool Steel Processed by Selective Laser Melting," *Metall. Mater. Trans. B*, vol. 46, no. 2, pp. 545–549, Apr. 2015.
[47] E. Pagounis, M. Talvitie, and V. K. Lindroos, "Influence of the metal/ceramic interface on the microstructure and mechanical properties of HIPed iron-based composites," *Compos. Sci. Technol.*, vol. 56, no. 11, pp. 1329–1337, Jan. 1996.

[48] J. R. Patel and M. Cohen, “Criterion for the action of applied stress in the martensitic transformation,” *Acta Metall.*, vol. 1, no. 5, pp. 531–538, Sep. 1953.
[49] E. Pagounis, E. Haimi, J. Pietikäinen, M. Talvitie, S. Vahvaselkä, and V. K. Lindroos, “Effect of thermal expansion coefficients on the martensitic transformation in a steel matrix composite,” *Scr. Mater.*, vol. 34, no. 3, pp. 407–413, Feb. 1996.
[50] W. B. Hanson, K. I. Ironside, and J. A. Fernie, “Active metal brazing of zirconia,” *Acta Mater.*, vol. 48, no. 18–19, pp. 4673–4676, Dec. 2000.
[51] T. Boegelein, S. N. Dryepondt, A. Pandey, K. Dawson, and G. J. Tatlock, “Mechanical response and deformation mechanisms of ferritic oxide dispersion strengthened steel structures produced by selective laser melting,” *Acta Mater.*, vol. 87, pp. 201–215, Apr. 2015.
[52] T. Boegelein, “Selective laser melting of a ferritic oxide dispersion strengthened steel,” 2000. [Online]. Available: https://livrepository.liverpool.ac.uk/2010620/. [Accessed: 26-Feb-2018].
[53] M. X. Zhang, Q. D. Hu, B. Huang, J. Z. Li, and J. G. Li, “Study of formation behavior of ZrC in the Fe–Zr–C system during combustion synthesis,” *Int. J. Refract. Met. Hard Mater.*, vol. 29, no. 5, pp. 596–600, Sep. 2011.
[54] H. Kotan, K. A. Darling, M. Saber, R. O. Scattergood, and C. C. Koch, “Thermal stability and mechanical properties of nanocrystalline Fe–Ni–Zr alloys prepared by mechanical alloying,” *J. Mater. Sci.*, vol. 48, no. 24, pp. 8402–8411, Dec. 2013.

Graphical abstract

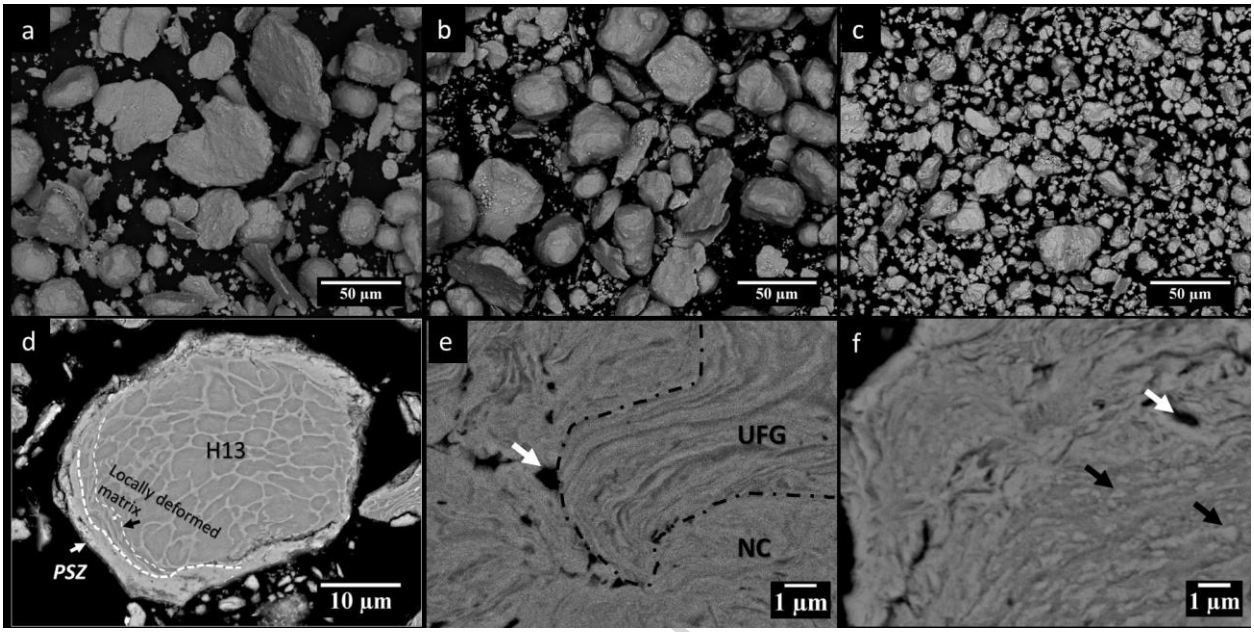

Highlights

- H13–partially stabilized zirconia nanocomposites were fabricated by selective laser melting
- Increasing the energy density generally enhanced densification
- All samples in the as-built condition showed a large amount of retained austenite
- Partially stabilized zirconia particles segregated under all processing conditions
- Fabricated nanocomposites have high hardness